

Simulation of three-dimensional free-surface dam-break flows over a cuboid, cylinder, and sphere

Zhihua Xie¹, Thorsten Stoesser², and Junqiang Xia³

¹Senior Lecturer, School of Engineering, Cardiff University, Cardiff, CF24 3AA, UK. E-mail: zxie@cardiff.ac.uk

²Professor, Department of Civil, Environmental and Geomatic Engineering, University College London, WC1E 6DE, UK. Email: t.stoesser@ucl.ac.uk

³Professor, State Key Laboratory of Water Resources and Hydropower Engineering Science, Wuhan University, Wuhan 430072, China. Email: xiajq@whu.edu.cn

ABSTRACT

A three-dimensional (3D) numerical study has been undertaken to investigate dam-break flows over 3D structures. A two-phase flow model has been developed within the large-eddy simulation (LES) framework. The governing equations have been discretised using the finite volume method, with the air-water interface being captured using a volume-of-fluid method whilst the Cartesian cut-cell method deals with complex geometries. The robustness and versatility of the proposed numerical approach are demonstrated first by applying it to a 3D dam-break flow over a cuboid. Good agreement is obtained between the simulation results and the corresponding experimental data and other numerical solutions. Then, a horizontal cylinder and a sphere are subjected to the same dam-break flow. Snapshots of water surface profiles are presented and discussed and turbulent vortical structures are identified in the flow. In addition, the pressure distribution around the structure, velocity field on the air-water interface, hydrodynamic loading on the structure, and energy dissipation during dam-break flow impact are analysed and discussed, providing more insight into such flows.

INTRODUCTION

Dam-break flows are an important phenomenon appearing in civil engineering applications potentially leading to severe flooding of communities downstream of the dam with catastrophic consequences, such as damage to buildings and infrastructure and loss of human life, such as the recent Michigan dam failure in May 2020. The hydraulics of dam-break flows (Costa and Schuster 1988) is affected by the mode of dam failure and how the failure propagates as a function of time, as well as its underlying complex topography and the presence of structures in its path. Dam-break flow interacting with structures results in complex three-dimensional (3D) hydrodynamics and substantial turbulence. In the past, significant advances have been made based on theoretical (Stoker 1957), experimental (Martin and Moyce 1952; Stansby et al. 1998; Janosi et al. 2004; Soares-Frazao and Zech 2008) and numerical studies of dam-break flows (Toro and Garcia-Navarro 2007). An ability to predict accurately the complex fluid-structure interaction of dam-break flows enables a better understanding of the resulting inundation and the structural response of buildings in a dam-break flows path.

Much effort has been devoted to develop numerical methods for dam-break flows. Commonly used are one-dimensional (1D) or two-dimensional (2D) depth-averaged shallow water equation (SWE) models, respectively and have been applied to simplified (Liang et al. 2006; Wu and Wang 2007) or realistic (Sleigh et al. 1998; Zhou et al. 2004; Liang and Borthwick 2009; Kesserwani and Liang 2010; Xia et al. 2010) domains, predicting fairly accurately flood inundation and horizontal velocities. Due to the assumption of hydrostatic pressure and depth-averaging of the velocity, SWE models are unable to provide the detailed near-field flow, and thus loadings and stresses around a structure immersed in a dam-break flow.

Continuous development of Computational Fluid Dynamics (CFD) methods and accompanied by constant increase in computer power have facilitated solving the Navier-Stokes equations (NSE) together with free surface calculations (McSherry et al. 2017). Various methods for dam-break flows have been developed for predicting the NSE together with the volume-of-fluid method on fixed (Lin and Xu 2006; Kleefsman et al. 2005) or adaptive (Greaves 2006; Pavlidis et al. 2016)

51 grids, the level set method (Yue et al. 2003), the smooth particle hydrodynamics (SPH) method
52 (Shao and Lo 2003; Gomez-Gesteira and Dalrymple 2004), and the non-hydrostatic model (Ai et al.
53 2011). In order to deal with complex topography and structures, body-fitted (Stoesser et al. 2008)
54 or unstructured grid (Pavlidis et al. 2016) and Cartesian grid method (Mittal and Iaccarino 2005;
55 Kara et al. 2015; Xie and Stoesser 2020a) can be used. Most dam-break flows and their interaction
56 with surrounding structures are turbulent, and therefore the effect of turbulence on the mean and
57 instantaneous flows needs to be considered unless all scales of turbulence are fully resolved. In
58 the past, the turbulence effect has been considered in several 3D dam-break flows based on the
59 Reynolds-averaged Navier–Stokes (RANS) equations (Yang et al. 2010; Marsooli and Wu 2014;
60 Munoz and Constantinescu 2020) or large-eddy simulation (LES) (Wu 2004; Wei et al. 2015) for
61 uneven beds or vertical structures (such as bridge piers or buildings).

62 Many SWE and 3D NSE models suffer from numerical instabilities near the free surface
63 (Kleefsman et al. 2005) which can be overcome by two-phase flow models, in which the air and
64 water phase are solved simultaneously. Such models have been employed for breaking waves (Xie
65 2012) and wave-structure interaction (Xie et al. 2020). When there is significant fluid-structure
66 interaction (FSI), air entrainment (Kiger and Duncan 2012) can become important, hence the
67 adoption of a two-phase flow model for FSI is preferred.

68 The objective of this study is therefore, to refine and validate a two-phase flow model (Xie 2012;
69 Xie 2015) using the newly developed Cartesian cut-cell method (Xie and Stoesser 2020a) and to
70 perform large-eddy simulations of 3D dam-break flows with complex structures with the aim to
71 predict accurately various quantities for dam-break flows impact on structures, such as water surface
72 elevations, water surface profiles, hydrodynamic loading on structures, and energy dissipation at
73 high temporal and spatial resolution.

74 **NUMERICAL FRAMEWORK**

75 The in-house LES code (Xdolphin3D) (Xie 2012; Xie 2015; Xie and Stoesser 2020a) is
76 employed in this study. The code solves the filtered Navier-Stokes equations on a staggered
77 Cartesian grid based on the finite volume method and the dynamic Smagorinsky subgrid-scale

78 model is employed to compute the unresolved scales of turbulence. A first-order or second-order
79 backward Euler method is used for the time derivative, which leads to an implicit scheme for the
80 Navier-Stokes equations and the PISO algorithm (Issa 1986) is employed for the pressure-velocity
81 coupling. In order to combine high-order accuracy with monotonicity, the advection terms are
82 discretised by a high-resolution scheme (Xie 2012), whereas central difference schemes are used
83 for the diffusion and pressure terms. In order to deal with complex geometries in Cartesian grids,
84 the 3D cut-cell method developed by Xie and Stoesser (2020a) is utilised in the finite volume
85 discretisation. Special treatment is needed in cut cells, for the advective and diffusive fluxes at cell
86 faces, as well as cell volumes. The high-resolution VOF scheme CICSAM (Compressive Interface
87 Capturing Scheme for Arbitrary Meshes) (Ubbink 1997) is used to capture the air-water interface,
88 which is defined as the volume fraction is equal to 0.5. The two-phase flow code has already been
89 extensively benchmarked and validated through a series of test cases for breaking waves (Xie 2012;
90 Xie 2015; Xie and Stoesser 2020b), LES studies of open-channel and free-surface flows over rough
91 beds (Xie et al. 2013a; Xie et al. 2013b; Xie et al. 2014; Xie et al. 2021) and moving bodies (Xie
92 and Stoesser 2020a), and wave-structure interaction (Xie et al. 2020).

93 **RESULTS AND DISCUSSION**

94 In this section, the results of dam-break flow simulations over a cuboid are presented first with
95 the goal to validate the present numerical approach. Once validated successfully a circular cylinder
96 and a sphere are subjected to the same dam-break flows with the goal to expand current knowledge
97 of dam-break-flow-structure interaction. Finally, the key parameters (hydrodynamic loads, energy
98 dissipation and mass conservation) are compared between three different structures subjected to
99 dam-break flows.

100 **Dam-break flow over a cuboid**

101 A dam-break flow over a cuboid, for which an experiment was carried out in the Maritime
102 Research Institute Netherlands (MARIN) (Kleefsman et al. 2005) is considered. The time history
103 of both the water surface elevation at several locations and the pressure on the cuboid were measured
104 in the experiment.

105 The LES is set up to replicate the laboratory tank, which was 3.22 m long, 1 m high and 1 m
106 wide (as shown in Fig. 1). A rectangular cuboid of 0.161(m) \times 0.161(m) \times 0.403(m) is placed
107 downstream of a water column with its initial height at 0.55 m. Two water surface gauges at the
108 front and back of the releasing gate, and four pressure transducers at the front and the top of the
109 cuboid are implemented during the simulation to sample numerical data that can be compared to
110 the experimental measurements. A uniform mesh 322 \times 100 \times 100 is used and the total number of
111 cells is 3.22 million. The velocity field is initialised as zero for both air and water with a hydrostatic
112 pressure and an adaptive time step with a maximum CFL number 0.2 is used in the simulation.

113 Fig. 2 shows snapshot of the predicted water surface profiles after the collapse of the water
114 column, together with the experimental measurement and the single-phase VOF model of Kleefsman
115 et al. (2005). It is shown that the water starts to collapse due to gravity and is almost two-dimensional
116 before it hits the box. A jet is formed at the front face of the box during the impact, moving upwards
117 and a little bit forward, whereas both sides wrap around the box and move towards the tank end.
118 The two leading edges impacts on the tank wall and move upwards and towards the centre. Some
119 of the water start to fall down on the wall due to gravity and some of the leading edges collide at
120 the centre to form a thin sheet moving back towards the obstacle. After impact, the water flows
121 back to the reservoir and complex air entrainment can be observed. It can be seen from Fig. 2 that
122 a good agreement is obtained between the snapshots of the present two-phase flow simulation and
123 the experiment as well as the single-phase flow model from Kleefsman et al. (2005).

124 In order to make quantitative comparison, the time histories of the water height at gauges H4
125 and H2 are compared with the experimental data and the single-phase flow model from Kleefsman
126 et al. (2005) in Fig. 3. Overall, both numerically obtained water heights agree reasonably well with
127 the experimental data. The mean absolute percentage errors between the present and experimental
128 results for gauges H4 and H2 are 4% and 7%, respectively. Slight discrepancies between mea-
129 surement and simulation at a later stage is observed at H2, which can be attributed to the complex
130 wave impact. Some phase difference can be observed and the wave propagation speed is not well
131 captured which might be partly due to the unresolved bed friction in the turbulent boundary layer,

132 and partly due to smaller air-bubbles being entrained into the flow not being captured with the
133 present mesh resolution.

134 Time history of the computed pressure as well as the measured and simulated pressure from
135 Kleefsman et al. (2005) at the front and top faces of the obstacle are plotted in Fig. 4. Generally,
136 convincing agreement between the two-phase flow simulation and experiment is obtained during
137 initial impact at the front face (P1 and P3). The peak pressure is well captured and the return wave
138 (around $t = 5$ s) can also be noticed although there is a phase shift as mentioned above. On the top
139 of the obstacle (P5 and P7), there are some oscillation for the pressure which is due to the complex
140 wave impact shown in Fig. 2. Overall, it can be observed that better agreement with the experiment
141 for the pressure field is obtained for the present two-phase flow approach, and there are no large
142 spurious spikes which are often observed in single-phase flow models as seen in Fig. 4 and also
143 Fig.11 in Marsooli and Wu (2014). Kleefsman et al. (2005) discussed that interpolation is needed
144 to get values in surface cells in the single-phase flow model, these spikes are caused by the surface
145 (or empty) cell changes to a fluid cell which the divergence is not zero. However, in the present
146 two-phase flow model, both air and water are solved and the divergence free is ensured for all the
147 cells in the computational domain and hence eliminates such pressure spikes.

148 **Dam-break flow over a horizontal cylinder**

149 In this section, a horizontal circular cylinder is subjected to a dam-break flow, which is often
150 observed in large woody debris dams for natural flood reduction and coastal flooding over pipelines.
151 This kind of flow is different from the commonly used vertical cylinder and this case can not be
152 studied by employing 2D SWE models. The computational setup and mesh is the same as that used
153 in the previous section, only the cuboid is replaced by a circular cylinder with the same height and
154 width as the cuboid (shown in Fig. 1).

155 Fig. 5 shows snapshots of the predicted water surface profiles during dam-break flow impact.
156 Compared to the cuboid case, it can be seen that a curved jet (at $t = 0.56$ s) is formed when the
157 water hits the cylinder due to the curvature of the surface. The jet overtops the cylinder with much
158 lower height than previous case, but moves further towards the tank wall. As a consequence, less

159 water comes around either side of the obstacle and the impact velocity for the leading edges is
160 smaller as observed from the height on the wall (at $t = 0.8$ s). After that ($t = 1.2 - 2.0$ s), the
161 water is reflected and returns back towards the reservoir with a similar pattern shown in Fig. 2.
162 For different geometry of the structures under the same dam-break flow, it is shown that the wave
163 impact is weaker for the circular cylinder case, which is due to the round edge during fluid-structure
164 interaction.

165 Fig. 6 shows water surface profiles and the streamwise velocity u along the central plane. At
166 the initial impact (at $t = 0.56$ s), the water surface profiles are similar for both cases whereas they
167 are significantly different in the vicinity of the structure. The streamwise velocity u is higher for
168 the cylinder case while the vertical velocity is higher for the cuboid case as the the jet is higher.
169 In front of the structure near the bed, the flow is reflected and it can be observed that the sign
170 of the streamwise velocity changes there. At $t = 0.8$ s, the jet moves faster for the cylinder case
171 with its height lower than the cuboid case. As more water pass by the cuboid (at $t = 1.2$ s), the
172 reflected velocity from the end wall is higher and the enclosed cavity is larger beneath the jet.
173 When the reflected wave returns to the structure (at $t = 2.0$ s), complex air-water interfaces can
174 be observed for both cases with air entrainment phenomena. The air cavity breaks up and a large
175 number of bubbles are formed when the reflected wave hits the structure. At this stage, the air-water
176 interface is unstable and has multiple length scales affected by the surface tension, turbulence and
177 mean flow. It can be seen from Fig. 2 and Fig. 5 that less bubbles entrained in the water and less
178 droplets are obtained for the cylinder case. It is worth noting that the two-phase flow model is
179 useful to study the detailed air entrainment phenomena. The air entrainment considered here is
180 less significant compared to dam spillways (white water phenomenon), which will require very fine
181 spatial resolution to capture the formulation and transport of a wide range of small bubbles and
182 their size distribution and is beyond the scope of this study.

183 **Dam-break flow over a sphere**

184 The computational setup and mesh are the same as the ones reported in the previous two
185 sections, with a sphere of similar cross sectional area (radius $r = 0.15$ m) to both the cuboid and

186 the cylinder is placed at the same location as before and subjected to the same dam-break flow as
187 shown in Fig. 1.

188 Fig. 7 shows the predicted water surface evolution and associated turbulent vortical structures,
189 which is plotted via isosurfaces of λ_2 (the second invariant of the velocity gradient tensor (Jeong
190 and Hussain 1995)), to identify vortex cores. Both oblique and top views are presented in order to
191 appreciate the complex 3D flow and turbulent structures. During initial impact ($t = 0.56$ s), there
192 is a pair of counter-rotating vortices developed in front of the sphere, as the flow is diverted by the
193 sphere. Large vortical structures are also observed in the vicinity of the air-water interface, with
194 opposite signs on either side of the sphere. At later stage ($t = 0.8$ s), two leading edges of the flow
195 hit the end of the tank and the water starts to overtop the sphere at lower water depth than for the
196 cuboid (Fig. 2) and the cylinder (Fig. 5) flows. At $t = 1.2$ s, the pair of counter-rotating vortices in
197 front of the sphere becomes weaker and moves a little bit backwards. When the wave is reflected
198 back from the end wall ($t = 2.0$ s), complex jet impingement and air entrainment can be observed,
199 associated with much stronger turbulent vortical structures both in the water and near the air-water
200 interface.

201 **Comparison between 3D structures**

202 Accurate prediction of hydrodynamic loads will lead to better understanding of the risk assess-
203 ment of infrastructure during dam-break flow and flooding events. The drag coefficient obtained
204 from the 3D model is useful to account for local losses due to 3D structures in depth-averaged
205 models. For different 3D structures, the hydrodynamic loads are normalised by the cross section
206 area in order to make comparison in the present study.

207 Fig. 8 shows the computed drag F_x (left) and lift F_y (right) forces on the three different structures
208 during the simulation. The forces increase suddenly when the water hits the structures and have
209 a local maximum at the initial stage. The horizontal force changes direction when the reflected
210 wave impacts on the structures (around $t = 1.5$ s), and remains in the positive streamwise direction
211 until the moment of the return flow hits the structures again (around $t = 5$ s). Compared to the
212 three cases, the cuboid has the highest horizontal force at the initial impact whereas the sphere

213 has the highest value when the first wave returned to the structures. The maximum force for the
214 sphere is higher during the reflected flow than the initial impact. Overall, the cuboid has the highest
215 horizontal force during the dam-break flow, and the maximum force is approximately 93% and
216 33% of that value for the cylinder and sphere, respectively.

217 For the vertical force, the curved surface (cylinder and sphere) always has a positive value
218 during the whole simulation as the flow attempts to lift these structures up. The negative vertical
219 force only occurs for the cuboid case when the returned flow hits the structure. Compared to the
220 three cases, the cylinder has the highest vertical force at the initial impact whereas the sphere has
221 the highest value at later stage. It is worth noting that the cuboid and sphere have similar maximum
222 vertical force during the initial impact, which is approximately 18% of the value for the cylinder
223 case.

224 In order to study the energy dissipation mechanism and mass conservation for the complex two-
225 phase flow during dam-break flow impact, the time history of the kinetic, potential, total energy,
226 and total mass are shown in Fig. 9, where the energy is calculated by integrating the region in
227 the water for the whole computational domain and normalised by the initial total energy. When
228 the water in the reservoir collapses, the potential energy decreases and transfers into the kinetic
229 energy. The kinetic energy achieves its maximum value during the flow impact on the structures
230 whereas the potential energy has a local minimum. The kinetic energy starts to decrease when the
231 flow passes over the structures and transfers some part back into the potential energy. There are
232 some fluctuation of the kinetic and potential energy at later stage and eventually the kinetic energy
233 will reduce to zero with potential energy converged to a certain value when the air-water interface
234 becomes flat. There is stronger energy dissipation from $t = 0 - 2$ s, which is mainly attributed to the
235 vorticity and turbulence generation during complex turbulent two-phase flows. During this time,
236 the sphere has the highest kinetic energy whereas the potential energy fluctuates between the three
237 cases. Overall, the total energy dissipation is highest for the cuboid case while it is lowest for the
238 sphere case which is due to the lower drag and lift forces. It is worth mentioning that comparison
239 for the energy dissipation is only for present computational setup with the same initial stage of

240 dam-break flows and similar volume of the structures. Different flow regime and different size of
241 structures might affect the energy dissipation, which is beyond the scope of this study.

242 Finally, mass conservation of the complex dam-break flow impact simulations is computed,
243 and it is found that the errors of the total mass during the simulations are less than 0.3% for all
244 cases considered here (shown in the last plot of Fig. 9), indicating a good mass conservation being
245 achieved for the present two-phase flow code.

246 **CONCLUSION**

247 In this study, a LES-based two-phase flow code Xdolphin3D has been introduced able to predict
248 3D dam-break flow-structure interaction. Different complex structures are well represented by the
249 Cartesian cut-cell method. Simulations of dam-break flow over cuboid have been qualitatively and
250 quantitatively compared with experimental measurements, with better agreement being obtained
251 from the present two-phase LES model and there are no large spurious spikes for pressure which
252 are often observed in single-phase flow models.

253 The free-surface flows during dam-break over a cuboid, cylinder, and sphere are presented
254 in detail, demonstrating the fully 3D flow field, which is difficult to study in SWE models. The
255 shape of the structures with similar volume has a significant effect on the free-surface flow field
256 for the same incoming dam-break flow, which in return will change the hydrodynamic loadings
257 and stresses around the structures. Different from single-phase flow over structures, it is found
258 that the hydrodynamic load changes with time regarding the dam-break flows and the cuboid has
259 the maximum drag force whereas the cylinder has the maximum lift force. Complex vortical
260 structures and air entrainment are generated during flow-structure interaction, which change the
261 energy dissipation associated with the flow.

262 **DATA AVAILABILITY STATEMENT**

263 Some or all data, models, or code that support the findings of this study are available from the
264 corresponding author upon reasonable request (numerical results and flow profiles).

ACKNOWLEDGEMENTS

Financial support was provided by the Royal Society Newton Advanced Fellowship (NAF/R1/201156), the EPSRC grants (EP/R022135/1 and EP/S016376/1), and Cardiff University GCRF project. Constructive comments from anonymous reviewers and the Associate Editor for the improvement of the manuscript are gratefully acknowledged.

REFERENCES

- Ai, C., Jin, S., and Lv, B. (2011). “A new fully non-hydrostatic 3d free surface flow model for water wave motions.” *International Journal for Numerical Methods in Fluids*, 66(11), 1354–1370.
- Costa, J. and Schuster, R. (1988). “The formation and failure of natural dams.” *Geological Society of America Bulletin*, 100(7), 1054–1068.
- Gomez-Gesteira, M. and Dalrymple, R. A. (2004). “Using a three-dimensional smoothed particle hydrodynamics method for wave impact on a tall structure.” *Journal of Waterway, Port, Coastal, and Ocean Engineering*, 130(2), 63–69.
- Greaves, D. M. (2006). “Simulation of viscous water column collapse using adapting hierarchical grids.” *International Journal for Numerical Methods in Fluids*, 50(6), 693–711.
- Issa, R. I. (1986). “Solution of the implicitly discretised fluid flow equations by operator-splitting.” *Journal of Computational Physics*, 62(1), 40–65.
- Janosi, I. M., Jan, D., Szabo, K. G., and Tel, T. (2004). “Turbulent drag reduction in dam-break flows.” *Experiments in Fluids*, 37, 219–229.
- Jeong, J. and Hussain, F. (1995). “On the identification of a vortex.” *Journal of Fluid Mechanics*, 285, 69–94.
- Kara, S., Kara, M. C., Stoesser, T., and Sturm, T. W. (2015). “Free-surface versus rigid-lid les computations for bridge-abutment flow.” *Journal of Hydraulic Engineering*, 141(9), 04015019.
- Kesserwani, G. and Liang, Q. (2010). “A discontinuous galerkin algorithm for the two-dimensional shallow water equations.” *Computer Methods in Applied Mechanics and Engineering*, 199(49), 3356 – 3368.

291 Kiger, K. T. and Duncan, J. H. (2012). “Air-entrainment mechanisms in plunging jets and breaking
292 waves.” *Annual Review of Fluid Mechanics*, 44, 563–596.

293 Kleefsman, K. M. T., Fekken, G., Veldman, A. E. P., Iwanowski, B., and Buchner, B. (2005). “A
294 volume-of-fluid based simulation method for wave impact problems.” *Journal of Computational
295 Physics*, 206(1), 363–393.

296 Liang, D., Falconer, R. A., and Lin, B. (2006). “Comparison between TVD-MacCormack and
297 ADI-type solvers of the shallow water equations.” *Advances in Water Resources*, 29(12), 1833 –
298 1845.

299 Liang, Q. and Borthwick, A. G. (2009). “Adaptive quadtree simulation of shallow flows with
300 wet-dry fronts over complex topography.” *Computers & Fluids*, 38(2), 221 – 234.

301 Lin, P. and Xu, W. (2006). “NEWFLUME: a numerical water flume for two-dimensional turbulent
302 free surface flows.” *Journal of Hydraulic Research*, 44, 79–93.

303 Marsooli, R. and Wu, W. (2014). “3-d finite-volume model of dam-break flow over uneven beds
304 based on vof method.” *Advances in Water Resources*, 70, 104 – 117.

305 Martin, J. C. and Moyce, W. J. (1952). “An experimental study of the collapse of liquid columns on
306 a rigid horizontal plane .4..” *Philosophical Transactions of the Royal Society of London Series
307 a-Mathematical and Physical Sciences*, 244(882), 312–324.

308 McSherry, R., Chua, K. V., and Stoesser, T. (2017). “Large eddy simulation of free-surface flows.”
309 *Journal of Hydrodynamics, Ser. B*, 29, 1–12.

310 Mittal, R. and Iaccarino, G. (2005). “Immersed boundary methods.” *Annual Review of Fluid
311 Mechanics*, 37, 239–261.

312 Munoz, D. H. and Constantinescu, G. (2020). “3-d dam break flow simulations in simplified and
313 complex domains.” *Advances in Water Resources*, 137, 103510.

314 Pavlidis, D., Gomes, J. L. M. A., Xie, Z., Percival, J. R., Pain, C. C., and Matar, O. K. (2016).
315 “Compressive advection and multi-component methods for interface-capturing.” *International
316 Journal of Numerical Methods in Fluids*, 80, 256–282.

317 Shao, S. and Lo, E. Y. (2003). “Incompressible sph method for simulating newtonian and non-

318 newtonian flows with a free surface.” *Advances in Water Resources*, 26(7), 787 – 800.

319 Sleight, P., Gaskell, P., Berzins, M., and Wright, N. (1998). “An unstructured finite-volume algorithm
320 for predicting flow in rivers and estuaries.” *Computers and Fluids*, 27(4), 479 – 508.

321 Soares-Frazaio, S. and Zech, Y. (2008). “Dam-break flow through an idealised city.” *Journal of*
322 *Hydraulic Research*, 46, 648–658.

323 Stansby, P. K., Chegini, A., and Barnes, T. C. D. (1998). “The initial stages of dam-break flow.”
324 *Journal of Fluid Mechanics*, 374, 407424.

325 Stoesser, T., Braun, C., Garcia-Villalba, M., and Rodi, W. (2008). “Turbulence structures in flow
326 over two-dimensional dunes.” *J. Hydraul. Eng.*, 134(1), 42–55.

327 Stoker, J. (1957). *Water waves*. Interscience Publishers, New York.

328 Toro, E. F. and Garcia-Navarro, P. (2007). “Godunov-type methods for free-surface shallow flows:
329 A review.” *Journal of Hydraulic Research*, 45(6), 736–751.

330 Ubbink, O. (1997). “Numerical prediction of two fluid systems with sharp interfaces.” Ph.D. thesis,
331 Imperial College of Science, Technology and Medicine, London, UK.

332 Wei, Z., Dalrymple, R. A., Héroult, A., Bilotta, G., Rustico, E., and Yeh, H. (2015). “Sph modeling
333 of dynamic impact of tsunami bore on bridge piers.” *Coastal Engineering*, 104, 26 – 42.

334 Wu, T. R. (2004). “A numerical study of three-dimensional breaking waves and turbulence effects.”
335 Ph.D. thesis, Cornell University, US.

336 Wu, W. and Wang, S. S. (2007). “One-dimensional modeling of dam-break flow over movable
337 beds.” *Journal of Hydraulic Engineering*, 133(1), 48–58.

338 Xia, J., Lin, B., Falconer, R. A., and Wang, G. (2010). “Modelling dam-break flows over mobile
339 beds using a 2d coupled approach.” *Advances in Water Resources*, 33(2), 171 – 183.

340 Xie, Z. (2012). “Numerical study of breaking waves by a two-phase flow model.” *Int. J. Numer.*
341 *Meth. Fluids*, 70(2), 246–268.

342 Xie, Z. (2015). “A two-phase flow model for three-dimensional breaking waves over complex
343 topography.” *Proc. R. Soc. A*, 471, 20150101.

344 Xie, Z., Lin, B., Falconer, R., Nichols, A.N. Tait, S., and Horoshenkov, K. (2021). “Large-eddy

345 simulation of turbulent free surface flow over a gravel bed.” *Journal of Hydraulic Research* ,
346 accepted.

347 Xie, Z., Lin, B., and Falconer, R. A. (2013a). “Large-eddy simulation of the turbulent structure in
348 compound open-channel flows.” *Adv. Water Res.*, 53, 66–75.

349 Xie, Z., Lin, B., and Falconer, R. A. (2014). “Turbulence characteristics in free-surface flow over
350 two-dimensional dunes.” *J. Hydro-Environ. Res.*, 8(3), 200–209.

351 Xie, Z., Lin, B., Falconer, R. A., and Maddux, T. B. (2013b). “Large-eddy simulation of turbulent
352 open-channel flow over three-dimensional dunes.” *J. Hydraul. Res.*, 51(5), 494–505.

353 Xie, Z. and Stoesser, T. (2020a). “A three-dimensional Cartesian cut-cell/volume-of-fluid method
354 for two-phase flows with moving bodies.” *Journal of Computational Physics*, 461, 109536.

355 Xie, Z. and Stoesser, T. (2020b). “Two-phase flow simulation of breaking solitary waves over
356 surface-piercing and submerged conical structures.” *Ocean Engineering*, 213, 107679.

357 Xie, Z., Stoesser, T., Yan, S., Ma, Q., and Lin, P. (2020). “A Cartesian cut-cell based multiphase flow
358 model for large-eddy simulation of three-dimensional wave-structure interaction.” *Computers
359 and Fluids*, 213, 104747.

360 Yang, C., Lin, B., Jiang, C., and Liu, Y. (2010). “Predicting near-field dam-break flow and impact
361 force using a 3d model.” *Journal of Hydraulic Research*, 48, 784–792.

362 Yue, W., Lin, C. L., and Patel, V. C. (2003). “Numerical simulation of unsteady multidimensional
363 free surface motions by level set method.” *International Journal for Numerical Methods in
364 Fluids*, 42, 853–884.

365 Zhou, J. G., Causon, D. M., Mingham, C. G., and Ingram, D. M. (2004). “Numerical prediction
366 of dam-break flows in general geometries with complex bed topography.” *Journal of Hydraulic
367 Engineering*, 130(4), 332–340.

List of Figures

368

369 1 Schematic of computational setup of a dam-break flow over a structure. Only the

370 cuboid is placed in the tank and it will be replaced with the cylinder and sphere for

371 different cases. 17

372 2 Snapshots of the dam-break flows of the single-phase flow model (left), experiment

373 (Kleefsman et al. 2005) (middle), and the present two-phase flow approach (right)

374 at t (s) = 0.4 (a), 0.56 (b), 0.8 (c), 1.2 (d), and 2.0 (e). The smaller pictures on the

375 top right inside the snapshots show the water in the reservoir. The water surfaces

376 are shown as the isosurface of volume fraction $F = 0.5$ and the single-phase and ex-

377 perimental snapshots are obtained from [http://www.math.rug.nl/~protect\](http://www.math.rug.nl/~protect/unhbox\voidb@x\protect\penalty\@M\{}veldman/comflow/dambreak.html)

378 [unhbox\voidb@x\protect\penalty\@M\{}veldman/comflow/dambreak.html](http://www.math.rug.nl/~protect/unhbox\voidb@x\protect\penalty\@M\{}veldman/comflow/dambreak.html). 18

379 3 Time history of the water height in the reservoir H4 (a) and in the tank H2 (b).

380 Present two-phase VOF model results are compared with the experimental and

381 single-phase VOF model results from Kleefsman et al. (2005). 19

382 4 Time history of the pressure at locations P1 (a), P3(b), P5(c) and P7 (d). Present

383 two-phase VOF model results are compared with the experimental and single-phase

384 VOF model results from Kleefsman et al. (2005). 20

385 5 Snapshots of the dam-break flow over a horizontal cylinder at t (s) = 0.56 (a), 0.8

386 (b), 1.2 (c), and 2.0 (d), where the water surfaces are shown as the isosurface of

387 volume fraction $F = 0.5$ 21

388 6 Comparison of the water surface profiles between the cuboid (left) and cylinder

389 (right) cases at t (s) = 0.56 (a), 0.8 (b), 1.2 (c), and 2.0 (d), where the water surface

390 is colored by the streamwise velocity u 22

391	7	Snapshots of the predicted water surface profile (shown as the isosurface of volume fraction $F = 0.5$) and turbulent vortical structure (colored by vertical vorticity component) at an oblique view (left panel) and top view (right panel) at t (s) = 0.56 (a), 0.8 (b), 1.2 (c), and 2.0 (d). Blue means negative vertical vorticity in which the flow moves clockwise and red means positive vertical vorticity in which the flow moves anti-clockwise.	23
392			
393			
394			
395			
396			
397	8	Time history of the drag (a) and lift (b) force acting on the cuboid, cylinder and sphere during the dam-break flow. The force is normalised by $1/2\rho ghA$, where A is the cross section area.	24
398			
399			
400	9	Time history of the normalised energy (a) and total mass (b) during the dam-break flow over a cuboid, cylinder and sphere.	25
401			

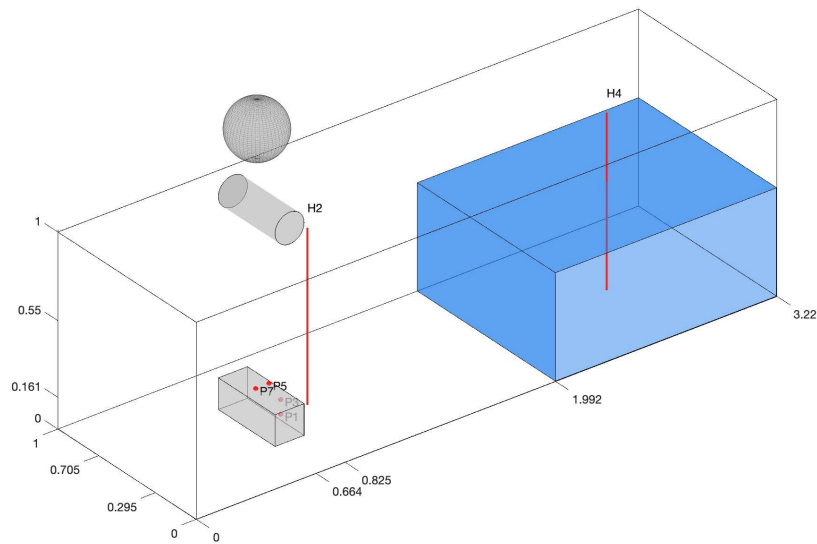


Fig. 1. Schematic of computational setup of a dam-break flow over a structure. Only the cuboid is placed in the tank and it will be replaced with the cylinder and sphere for different cases.



(a) $t = 0.4$ s



(b) $t = 0.56$ s



(c) $t = 0.8$ s



(d) $t = 1.2$ s



(e) $t = 2.0$ s

Fig. 2. Snapshots of the dam-break flows of the single-phase flow model (left), experiment (Kleefsman et al. 2005) (middle), and the present two-phase flow approach (right) at t (s) = 0.4 (a), 0.56 (b), 0.8 (c), 1.2 (d), and 2.0 (e). The smaller pictures on the top right inside the snapshots show the water in the reservoir. The water surfaces are shown as the isosurface of volume fraction $F = 0.5$ and the single-phase and experimental snapshots are obtained from <http://www.math.rug.nl/~veldman/comflow/dambreak.html>.

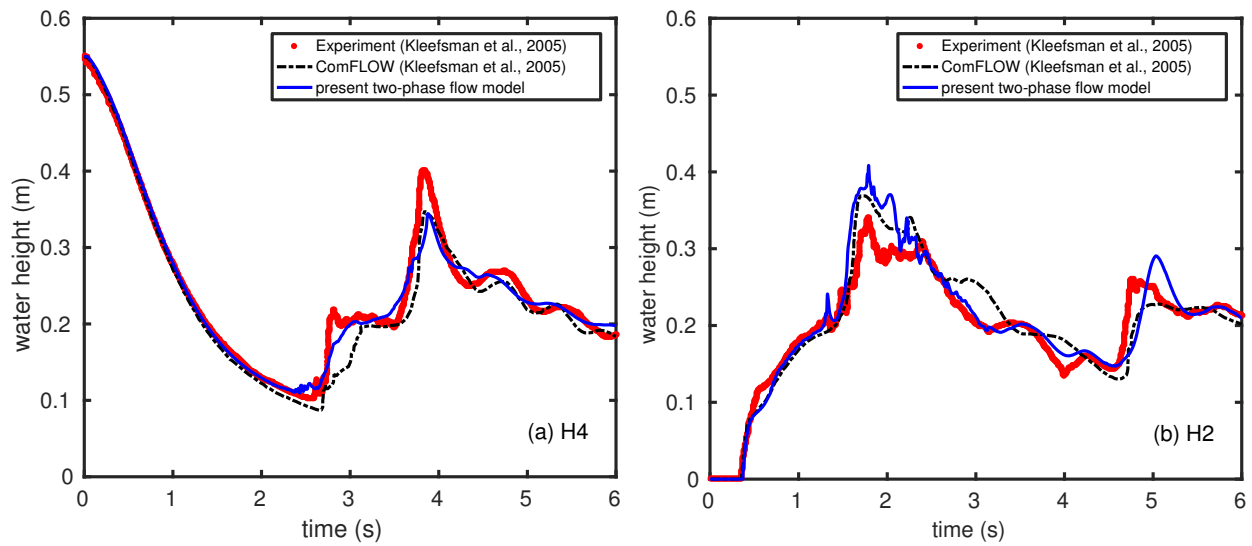


Fig. 3. Time history of the water height in the reservoir H4 (a) and in the tank H2 (b). Present two-phase VOF model results are compared with the experimental and single-phase VOF model results from Kleefsman et al. (2005).

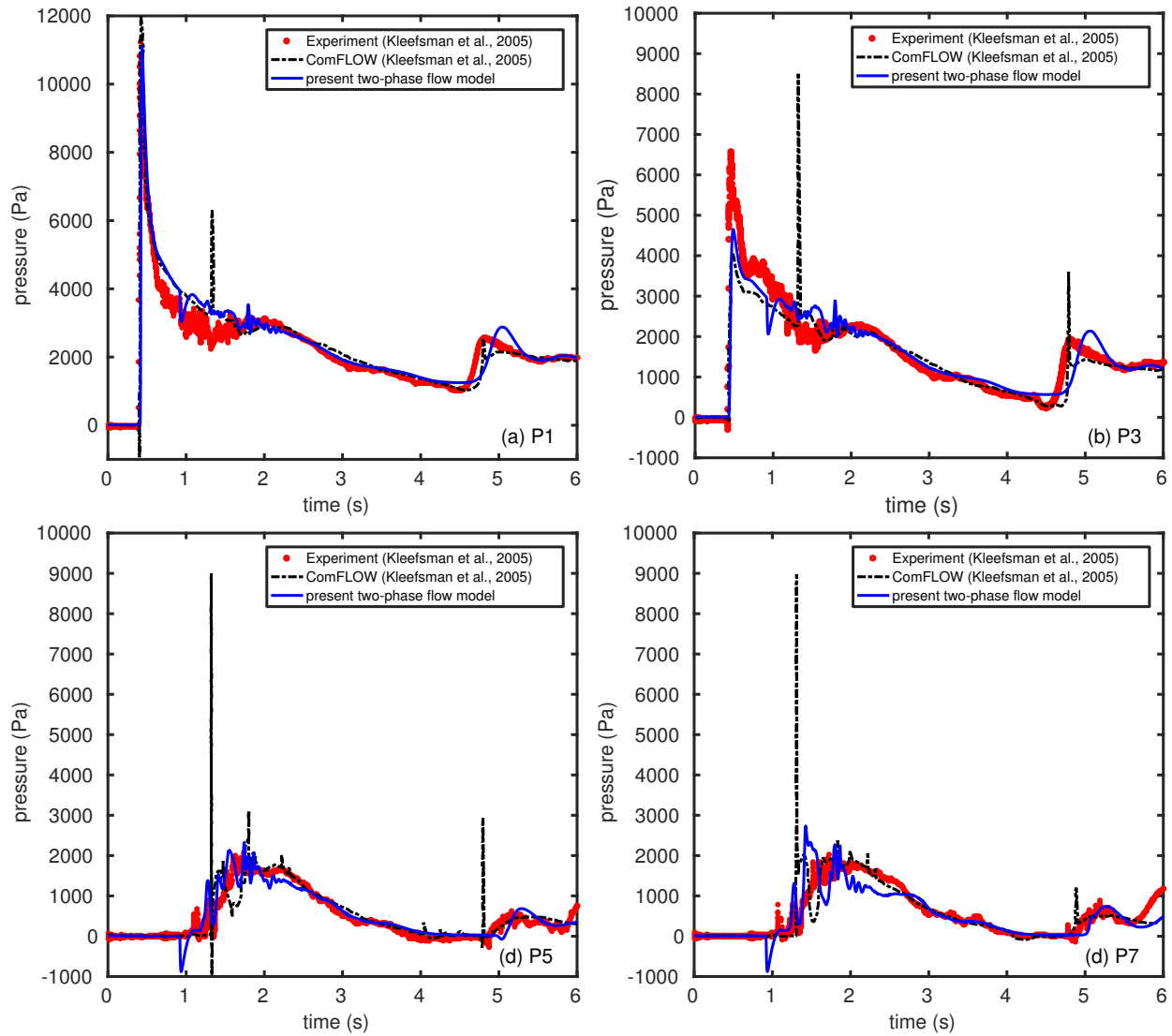


Fig. 4. Time history of the pressure at locations P1 (a), P3(b), P5(c) and P7 (d). Present two-phase VOF model results are compared with the experimental and single-phase VOF model results from Kleefsman et al. (2005).

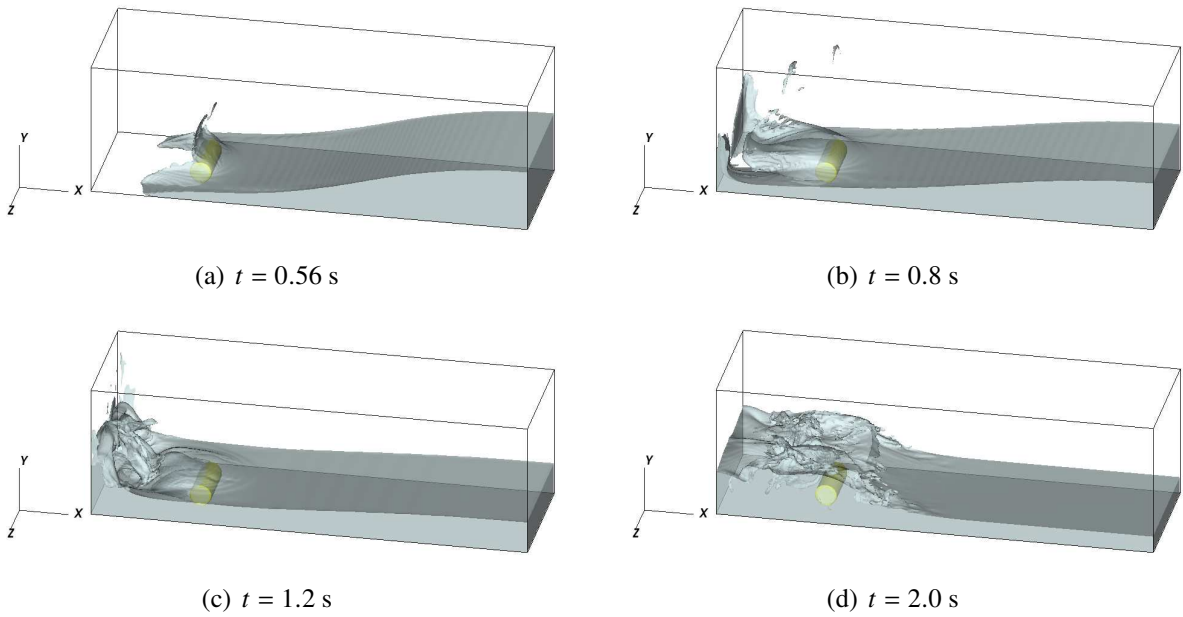


Fig. 5. Snapshots of the dam-break flow over a horizontal cylinder at t (s) = 0.56 (a), 0.8 (b), 1.2 (c), and 2.0 (d), where the water surfaces are shown as the isosurface of volume fraction $F = 0.5$.

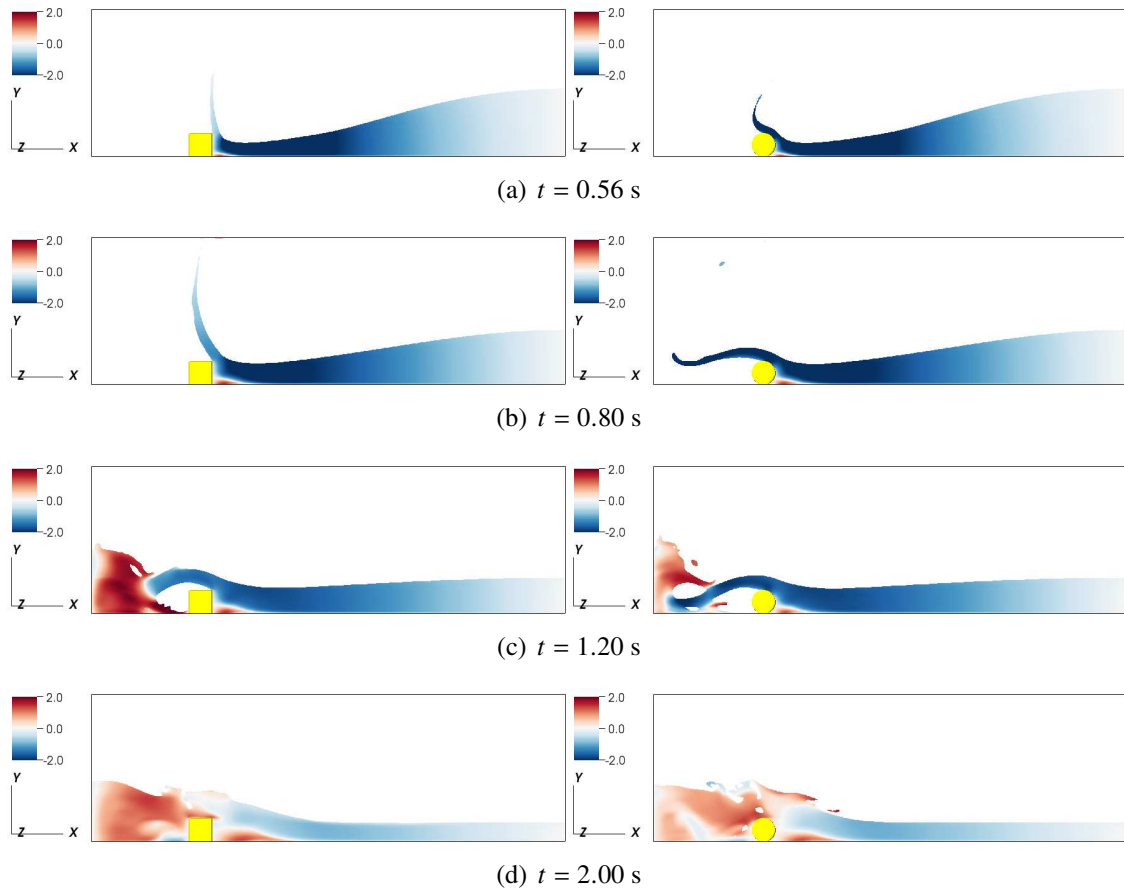


Fig. 6. Comparison of the water surface profiles between the cuboid (left) and cylinder (right) cases at t (s) = 0.56 (a), 0.8 (b), 1.2 (c), and 2.0 (d), where the water surface is colored by the streamwise velocity u .

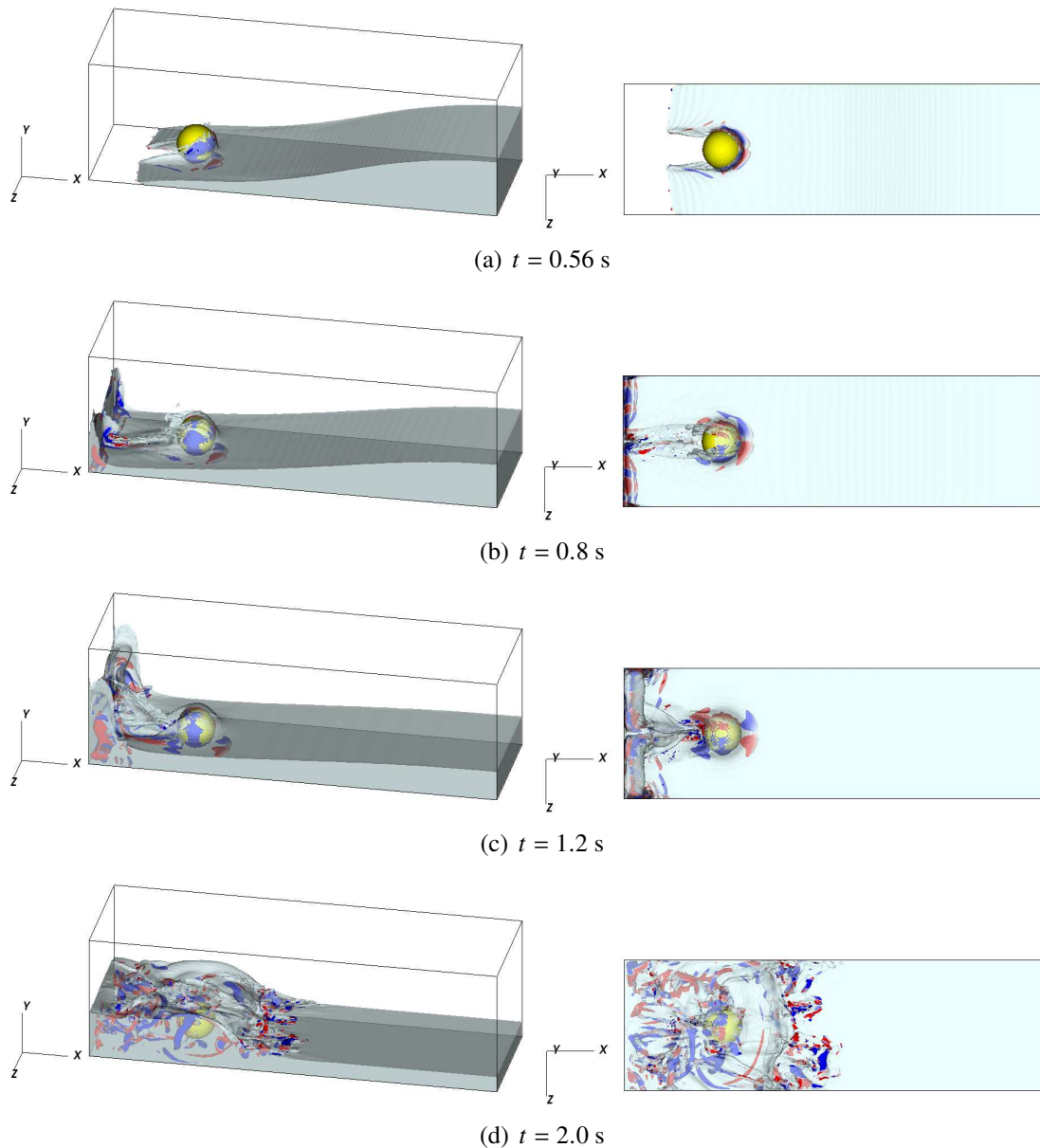


Fig. 7. Snapshots of the predicted water surface profile (shown as the isosurface of volume fraction $F = 0.5$) and turbulent vortical structure (colored by vertical vorticity component) at an oblique view (left panel) and top view (right panel) at t (s) = 0.56 (a), 0.8 (b), 1.2 (c), and 2.0 (d). Blue means negative vertical vorticity in which the flow moves clockwise and red means positive vertical vorticity in which the flow moves anti-clockwise.

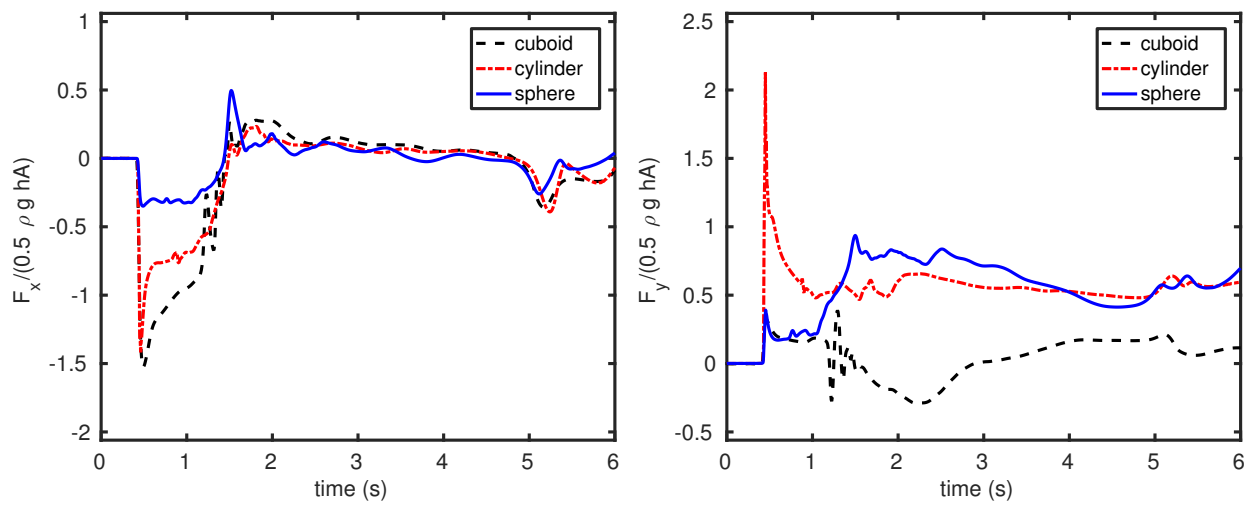


Fig. 8. Time history of the drag (a) and lift (b) force acting on the cuboid, cylinder and sphere during the dam-break flow. The force is normalised by $1/2\rho ghA$, where A is the cross section area.

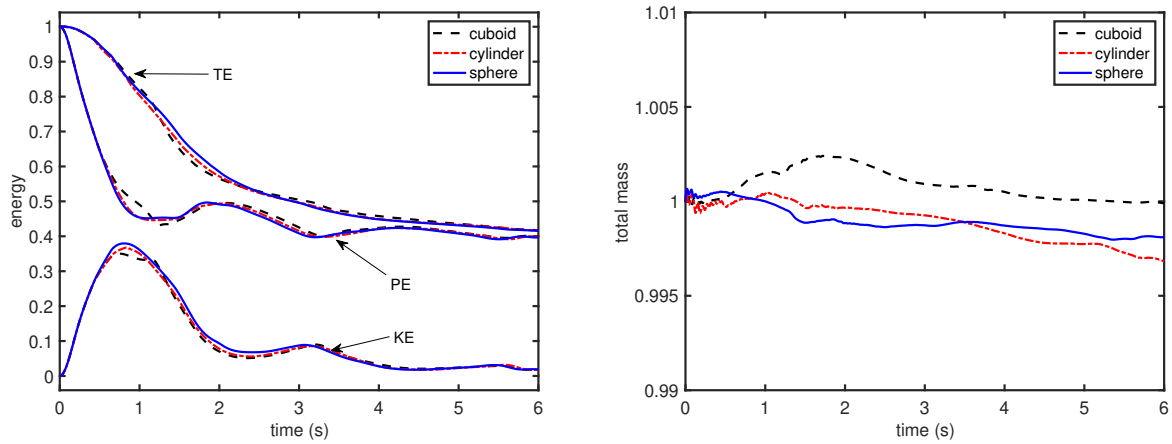


Fig. 9. Time history of the normalised energy (a) and total mass (b) during the dam-break flow over a cuboid, cylinder and sphere.